Stress-Induced Martensitic Transformation in Na_3YCl_6

Akira Miura[a+*], Koki Muraoka[b+*], Kotaro Maki[c], Saori Kawaguchi[d], Kazuhiro Hikima[e], Hiroyuki Muto[e,f], Atsunori Matsuda[e], Ichiro Yamane[c], Toshihiro Shimada[a], Hiroaki Ito[c], Yoshikazu Mizuguchi[g], Chikako Moriyoshi,[h] Hiroshi Nakajima,[i] Shigeo Mori,[i] Hiroshi Oike,[j] Akira Nakayama,[b] Wenhao Sun,[k] Nataly Carolina Rosero-Navarro,[a,l], Kiyoharu Tadanaga[a]

[+]contributed equally

[a] Faculty of Engineering, Hokkaido University, Kita 13, Nishi 8, Sapporo 060-8628, Japan

[b] Department of Chemical System Engineering, The University of Tokyo, 7-3-1 Hongo, Bunkyo-ku, Tokyo 113-8656, Japan

[c] Graduate School of Chemical Science and Engineering, Hokkaido University, Kita 13, Nishi 8, Sapporo 060-8628, Japan

[d] Japan Synchrotron Radiation Research Institute, Sayo, Hyogo 679-5198, Japan

[e] Department of Electrical and Electronic Information Engineering, Toyohashi University of Technology, 1-1 Hibarigaoka, Tempaku, Toyohashi, Aichi 441-8580, Japan

[f] Institute of Liberal Arts and Sciences, Toyohashi University of Technology, 1-1 Hibarigaoka, Tempaku, Toyohashi, Aichi 441-8580, Japan

[g] Department of Physics, Tokyo Metropolitan University, Hachioji 192-0397, Japan

[h] Graduate School of Advanced Science and Engineering, Hiroshima University, 1-3-1 Kagamiyama, Higashihiroshima, 739-8526, Japan

[i] Department of Materials Science, Graduate School of Engineering, Osaka Metropolitan University, 1-1 Gakuen-cho, Naka-ku, Sakai, Osaka 599-8531, Japan

[j] PRESTO, Japan Science and Technology Agency, 4-1-8 Honcho, Kawaguchi 332-0012, Japan

[k] Department of Materials Science, University of Michigan, Ann Arbor, Michigan 48109, United States

[l] Instituto de Cerámica y Vidrio (CSIC), Campus de Cantoblanco, 28049, Madrid, Spain

Email: amirua@eng.hokudai.ac.jp (AMiura) , muraok_k@chemsys.t.u-tokyo.ac.jp (KMuraoka)

KEYWORDS: martensitic transformation, uniaxial pressure, volume expansion, monoclinic, rhombohedral, ternary sodium chloride

ABSTRACT: Martensitic transformation with volume expansion plays a crucial role in enhancing the mechanical properties of steel and partially stabilized zirconia. We believe that a similar concept could be applied to unexplored non-oxide materials. Herein, we report the stress-induced martensitic transformation of monoclinic Na_3YCl_6 with ~3.4% expansion. In-situ synchrotron X-ray diffraction and atomistic simulations showed that the anisotropic crystallographic transformation from monoclinic to rhombohedral Na_3YCl_6 occurs exclusively under uniaxial pressure; no effect is observed under hydrostatic pressure conditions. The uniaxially-pressed powder compact of monoclinic Na_3YCl_6 showed a large indentation impression and low Young's modulus, in contrast to its high bulk modulus, suggesting that these unique mechanical properties are induced by the martensitic transformation.

1. Introduction

In the past decade, halide materials have gathered significant attention as prospective materials for sustainable energy storage systems;[1-6] for example, chloride electrolytes fabricated by cold sintering can be used in all-solid-state batteries. However, the volume changes of the cathode and anode after repeated charge–discharge cycles reduce the battery capacity. Hence, the mechanical properties of halide materials, such as low Young's modulus, are critical for their processing and durability; their improvement is essential for developing next-generation materials with high reliability. However, strategies to improve the mechanical properties of halide crystals have rarely been reported.

Partially stabilized zirconia (PSZ) is a ceramic material used in engineering ceramics, high-temperature coatings, and bio and dental ceramics. The high strength and toughness of PSZ originate from its stress-induced phase transformation with significant volume expansion. This phase transformation without long-range atomic diffusion is a form of martensitic transformation. Although such stress-induced martensitic transformation with volume expansion is expected to occur in other ceramics, PSZ is the only example in practical oxide.[7, 8] In the present study, we explored the possibility of stress-induced martensitic transformation with volume expansion in a relatively unexplored class of materials: highly ionic halide materials, which can improve their mechanical properties.

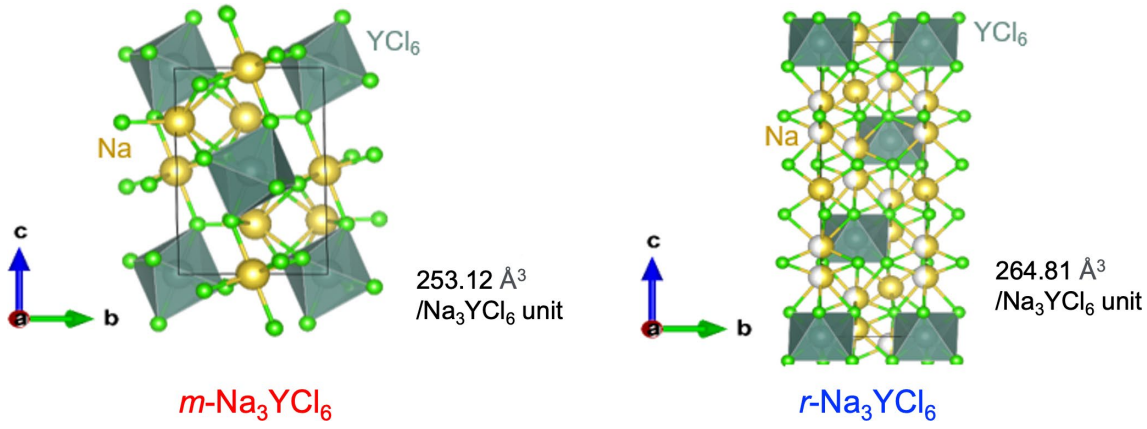

Figure 1. Crystal structures of *m*- and *r*-Na_3YCl_6.

Na_3YCl_6 is a ternary sodium chloride with two polymorphs: monoclinic and rhombohedral (Fig. 1). The monoclinic Na_3YCl_6 (*m*-Na_3YCl_6) is a high-density phase composed of a YCl_6 octahedron and a distorted $NaCl_6$ octahedron.[9-11] The rhombohedral Na_3YCl_6 (*r*-Na_3YCl_6) is a low-density phase composed of a YCl_6 octahedron and three $NaCl_6$ octahedra. The unique structural feature of *r*-Na_3YCl_6 is the $NaCl_6$ octahedra with partially occupying Na sites, which is also the reason for its low density.[12] Upon slow cooling, *m*-Na_3YCl_6 transforms to *r*-Na_3YCl_6

accompanied with volume expansion; in other words, negative thermal expansion is shown by the phase transformation.[12] This phase transition is expected to affect the mechanical properties of *m*-Na_3YCl_6, similar to the case of tetragonal ZrO_2 (which also exhibits a phase transition to monoclinic ZrO_2 with large volume expansion upon cooling).[13]

Herein, we report the martensitic transformation of *m*-Na_3YCl_6 to *r*-Na_3YCl_6 with an anisotropic volume expansion induced by an external stress and the extreme softness of *m*-Na_3YCl_6.

2. Experimental and Computational Methods

All the experimental procedures were performed under non-atmospheric pressure. NaCl and YCl_3 were weighed in a 3:1 molar ratio and mixed by hand for 15 min. The mixed sample was sealed in a quartz tube. The *m*-Na_3YCl_6 and *r*-Na_3YCl_6 samples were synthesized by heating at 400 °C for 50 h and 700 °C for 10 h, respectively. To study the stress-induced phase transition, the synthesized *m*-Na_3YCl_6 was subjected to a pressure of 0.3 GPa in a hydraulic press.

The crystal structures were visualized using the Visualization for Electronic Structural Analysis software.[14] X-ray diffraction (XRD) measurements were performed using a Miniflex600 diffractometer (Rigaku) without exposure to air. Rietveld refinement was performed by SmartLab Studio II (Rigaku) or TOPAS software.[15] The pressure-dependent phase transition was investigated on BL10XU at SPring-8 (2022A1323). The samples were pressurized in a diamond anvil cell, and helium gas was used as the pressure medium. The wavelength of the X-ray was 0.412859 Å, and the pressure was calculated from the Raman shift of ruby. The temperature dependence was measured on BL02B2 at SPring-8.[16] The sample was sealed by a quartz capillary, and the temperature was controlled using heated nitrogen gas. The wavelengths used were 0.496480 (2022A1296) or 0.496571 Å (2022A1323). The transmission electron microscopy (TEM) measurements were performed using a JEM-2100F electron microscope (JEOL Co., Ltd.) at an acceleration voltage of 200 kV. The powder specimen was dispersed on a TEM grid that was attached to a vacuum transfer holder. The impedance measurement was performed using an impedance analyzer (Biologic SP-200) in the frequency range of 0.1 Hz to 10 MHz at an amplitude of 10 mV. The mechanical properties of the *m*- and *r*-Na_3YCl_6 powder compact produced by uniaxial pressing was measured using a Tensilon universal material testing instrument (RTF-1250, A&D Company, Ltd.).[17] The indentation impression after acute-angle indentation was observed by scanning electron microscopy (SEM; IT-200, JEOL).

The stability and reaction energy were calculated using the Generalized Solid-State Nudged Elastic Band (G-SSNEB) method[18] with PreFerred Potential (PFP) version 4.0.0.[19] Since part of the Na sites in the *r*-phase is disordered, we considered two atomistic models, namely *r*-1 and *r*-2. A major challenge in modeling this solid–solid phase transition by simulation is finding atom-to-atom mapping between the *r*- and *m*-phases. The mapping is not intuitively obvious primarily because the shapes of the two cells are largely different; hence, we employed a structure-matching method developed by Stevanović et al.[20] The algorithm first explores all the possible combinations of unit cell vectors and all the isomeric transformations of the two given cells to find the supercells with the largest volumetric overlap. Then, all the possible combinations of symmetry operations, site at origin, and permutation of atom indices are explored to find the best atom-to-atom mapping with a minimum number of dissociations of chemical bonds and minimum total distances. We optimized the supercell models for *m*, *r*-1, and *r*-2 structures until the maximum forces became less than 0.01 eV/Å. The lattice matrices of the *r*- and *m*-phases were diagonalized to confirm that the shrinkage indeed occurs along the *c* axis of the supercell model. We utilized the G-SSNEB method under either isotropic pressure of 0.5 GPa, anisotropic pressure of 0.5 GPa, or no pressure until the maximum forces were reduced to less than 0.03 eV/Å. Plane-wave, periodic density functional theory (DFT) calculations using Perdew-Burke-Ernzerhof functional were performed to compute single point energies for images in G-SSNEB with the Vienna Ab initio Simulation Package,[21] version 6.1.2. We used Pymatgen to

generate a *k*-point mesh of 100 per reciprocal atom[22] with a self-consistent field convergence criteria of 10^{-6} eV and a cutoff energy of 520 eV. The potential energy of PFP was differentiated to yield elastic tensors, and Hill's approximation was employed to calculate the Young's modulus.

3. Results and Discussion

The *m*- and *r*-Na_3YCl_6 samples were synthesized at different temperatures. The structures of the different samples characterized by synchrotron XRD were found to be close to the reported structures (Fig. S1, Table S1 and CIF files).[9-12] The ion conductivity of *m*-Na_3YCl_6 obtained from the impedance measurement was 6×10^{-6} S cm^{-1}, comparable to the reported value.[10]

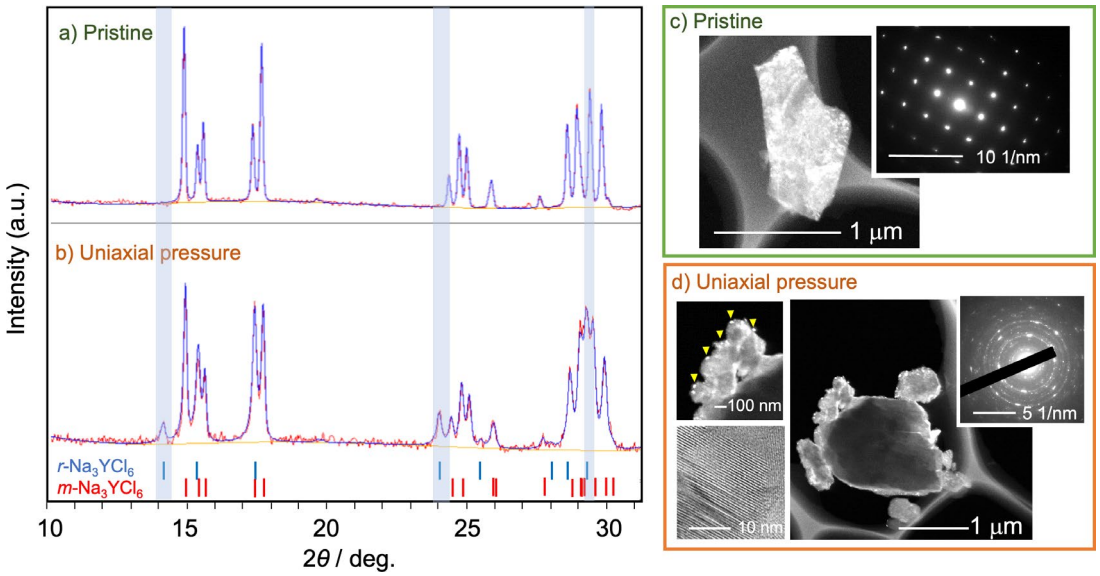

Figure 2. Phase transformation of *m*-Na_3YCl_6 triggered by uniaxial pressurization. X-ray diffraction patterns of *m*-Na_3YCl_6 (a) before uniaxial pressurization and (b) after applying a uniaxial pressure of 0.3 GPa by the hydraulic press. The blue highlighted regions show the representative peaks of *r*-Na_3YCl_6. The blue and red bars represent the Bragg peak positions of *r*-Na_3YCl_6 and *m*-Na_3YCl_6, respectively. The red and blue lines correspond to experimental and simulated diffraction patterns, respectively. Transmission electron microscopy images and electron diffraction patterns of *m*-Na_3YCl_6 (c) before mechanical stimulation and (d) after uniaxial pressurization. The yellow triangles highlight nanoparticles of ~10 nm in size.

The XRD pattern of *m*-Na_3YCl_6 before the mechanical stimulation shows peaks corresponding to only *m*-Na_3YCl_6 (Fig. 2a). The hydraulic pressure of 0.3 GPa transforms 28.2 % of the *m*-phase to *r*-phase as evident from the Rietveld refinement (Fig. 2b). The TEM image of pristine *m*-Na_3YCl_6 (Fig. 2c) shows microparticles with a spotted electron diffraction pattern, indicative of its high crystallinity. The conversion of approximately one-third of the *m*-phase implies that uniaxial pressurization along a specific axis of the *m*-phase induces the phase transformation, assuming that the crystallites are randomly oriented in the powder. The TEM images show a part of the *m*-phase (Fig. 2c) that turned into nanoparticles with diameters of ~10 nm after pressurization (Fig. 2d). The crystalline fringes observed in the high-resolution TEM image of these nanoparticles and the Debye–Scherrer ring observed in the electron diffraction pattern confirm their crystalline nature (Fig. 2d). Owing to the similar structures and limitation of the resolution of electron diffraction, discerning whether the newly appeared nanoparticles and the coexisting microparticles (in Fig. 2d) correspond to *m*- or *r*-phases is difficult (Fig. S3); however, we speculate that *r*-Na_3YCl_6 comprises micro and nanoparticles. This is because rhombohedral structures are detected only after the mechanical stimulation and formation of nanoparticles, and a small amount of these nanoparticles cannot account for 28.2 % of the *r*-phase.

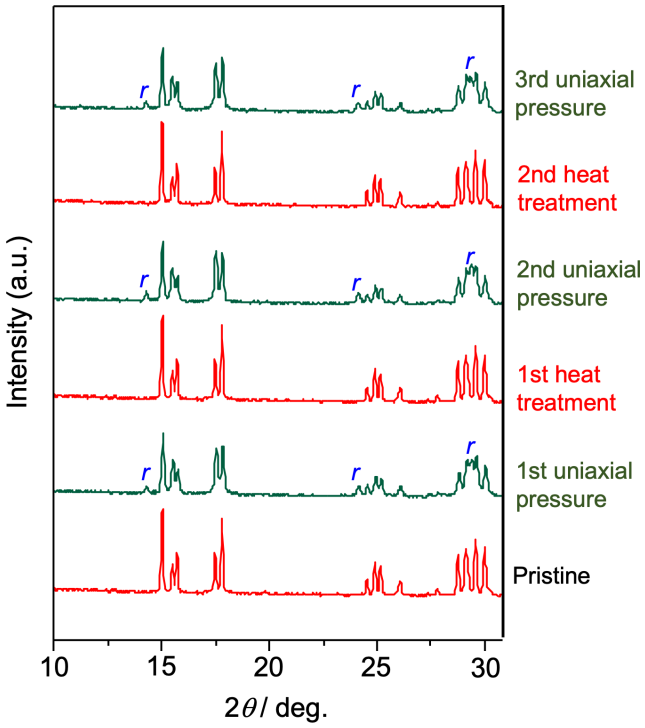

Figure 3. Phase-transformation cycling obtained by successive application of uniaxial pressure and temperature. X-ray diffraction patterns of *m*-Na_3YCl_6 after applying a uniaxial pressure of 0.3 GPa and subsequent heating at 400 °C; *r* indicates the rhombohedral phase.

While the backward transformation from *r*- to *m*-phase by the application of pressure (Fig. S4) was not significant, the transformed *r*-phase reverted to *m*-phase upon heating at 100–180 ° C, as evident from in-situ XRD studies (Fig. S5). The XRD patterns in Fig. 3 confirm the phase-transformation cycling between *m*- and *r*-phases by applying successive uniaxial pressure and heating.

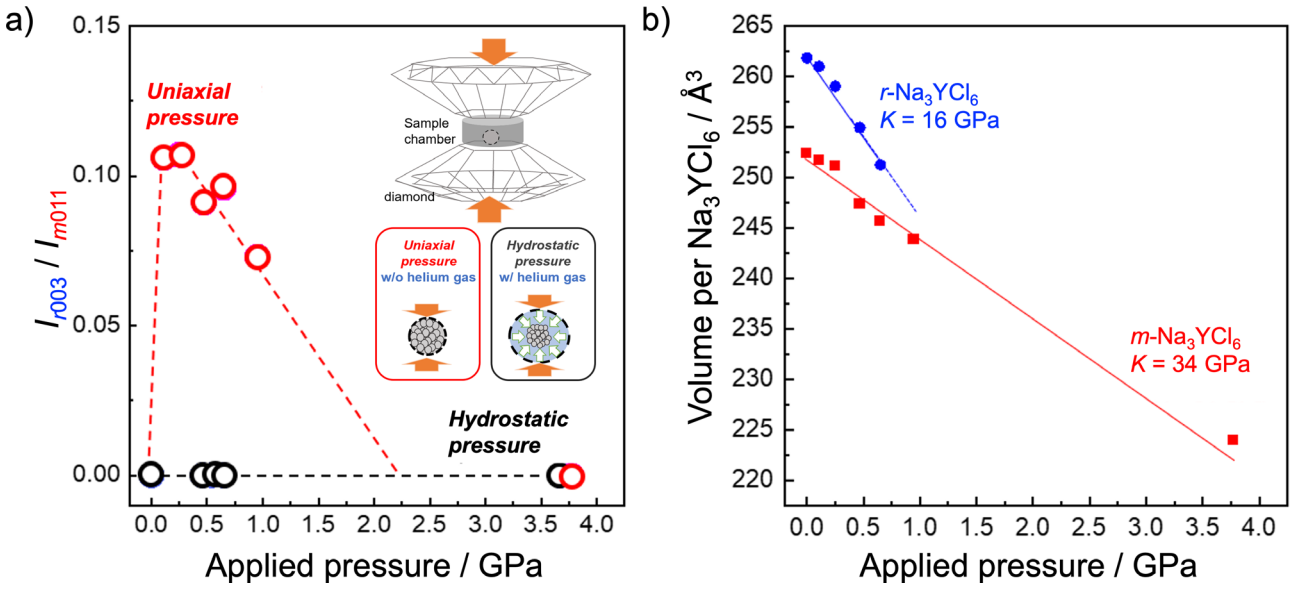

Figure 4. High-pressure synchrotron X-ray diffraction study of *m*-Na_3YCl_6. a) Intensity ratios of the (003) diffraction peak in *r*-Na_3YCl_6 to the (011) diffraction peak in *m*-Na_3YCl_6 under uniaxial pressure without helium gas or hydrostatic pressure with helium gas as the pressure medium. b) Lattice volumes of *m*- and *r*-Na_3YCl_6 and their bulk moduli calculated from the diffraction peaks.

An intriguing point in the uniaxial-pressure-induced *m*-to-*r* phase transformation of Na_3YCl_6 is that the starting *m*-phase is denser than the resulting *r*-phase; the lattice volume of *m*- and *r*-phases are 253.12 and 261.84 Å^3/Na_3YCl_6, respectively. This means that ~3.4 % volume expansion is achieved by applying a relatively weak force. Thermodynamic principles largely preclude the possibility that isotropic pressure causes transformation to denser phases. To confirm this, we used atomistic simulations to compare the stability of the *m*- and *r*-phases under different isotropic pressure conditions. As shown in Fig. S6, the application of isotropic pressure monotonically stabilizes the denser *m*-phase more, confirming that the high-density *m*-phase is more stable under isotopically pressurized conditions. A transition from *r*- to *m*-phase under isotropic pressure has been reported in isostructural Ag_3YCl_6.[23]

Hence, we hypothesize that the phase transition is caused by uniaxial stress and not by isotropic pressure. For validation, we recorded in-situ synchrotron XRD patterns of *m*-Na_3YCl_6 under uniaxial and hydrostatic (i.e. isotropic) pressures (Figs. 4 and S7). The uniaxial pressurization of the *m*-phase results in the appearance of peaks corresponding to the *r*-phase at 0.11 GPa (Fig. 4a), confirming the unusual pressure-induced phase transformation from a denser to a sparser phase. As the uniaxial pressure is increased above 0.50 GPa, the peak ratio of *r*- to *m*-phase decreases and disappears at 3.7 GPa, indicating that the high-density *m*-phase is stable with increase in pressure. Conversely, the application of hydrostatic pressure did not show any signs of the phase transformation. This supports the hypothesis that uniaxial stress triggers the unique phase transformation of *m*-Na_3YCl_6 to *r*-Na_3YCl_6. Fig. 4b shows the pressure-dependent lattice volumes recorded by in-situ XRD under uniaxial pressure. With increase in the pressure, the volumes of both the phases decrease.

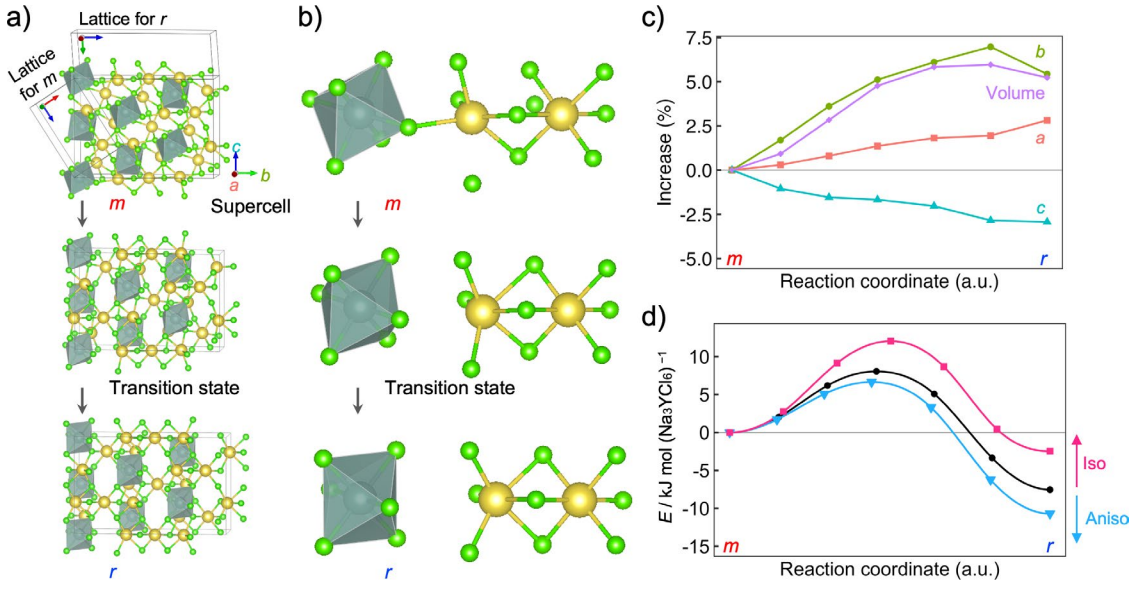

Figure 5. Calculated martensitic transformation pathway and volume change. a) Relationships between the *m*-phase, *r*-phase, and supercell model for phase transformation. b) Schematic of the local structure change of Na_3YCl_6 from *m*- to *r*-phase. c) Variations of lattice constants and volumes during the phase transformation of Na_3YCl_6 from *m*- to *r*-phase at zero pressure. d) Energy profiles of the phase transformation of Na_3YCl_6 from *m*- to *r*-phase. The black circles represent the transformation without pressure, while the blue triangles and red squares represent the transformations under uniaxial and hydrostatic pressures, respectively.

The atomistic simulation was performed to understand the transformation pathway. The phase transformations under no pressure were obtained by the G-SSNEB method[18] using the universal neural network potential (Fig. 5). The accuracy of the potential was confirmed by DFT calculations (Table S2 and Fig. S8). We constructed supercell models converted from monoclinic and rhombohedral structures (Fig. 5a) and calculated two transformation routes for the half-occupied Na sites in the rhombohedral structure (Fig. S9). As the routes are nearly identical, only one is shown (Fig. 5). The *m*-phase is slightly thermodynamically unfavorable than the *r*-phase under no pressure (Figs. 5d and S6). Thus, the *m*-phase is metastable, and the kinetic barrier prevents the transformation to the *r*-phase. During the *m*-to-*r* transformation, YCl_6 octahedra rotates, and Na atoms translate to form vacancy sites (Fig. 5b). This structural transformation involves ~2.5 % reduction in the *c* axis and 2.5–5 % expansion in the *a* and *b* axes (Fig. 5c). Consequently, the volume expands by approximately 5 %. Therefore, this phase transformation is martensitic, characterized by highly anisotropic lattice shrinkage and expansion.

Considering that the uniaxial pressure transformed approximately one-third of the *m*-phase to the *r*-phase (Fig. 2b), we surmised that the phase transformation occurs when the pressure is along a specific axis of the crystallites. Because the *c* axis of the supercell is the only shrunken axis during the transformation (Fig. 5c), we performed the G-SSNEB calculation with the pressure applied along that axis. Strikingly, the axial pressure lowered the activation energy and increased the energy difference between the starting and resulting phases (Fig. 5d). These effects promote the *m*-to-*r* phase transformation of Na_3YCl_6. In contrast, the same calculation under hydrostatic pressure increased the activation energy and decreased the energy difference, making this transformation kinetically and thermodynamically unfavorable (Fig. 5d). This result is remarkably consistent with the experimental observation (no phase transformation under hydrostatic pressure; Fig. 4a). The effect of different external pressures on the phase transformation is presented in Fig. S10 in the Supporting Information. These results support that the uniaxial force causes the unique martensitic transformation of Na_3YCl_6.

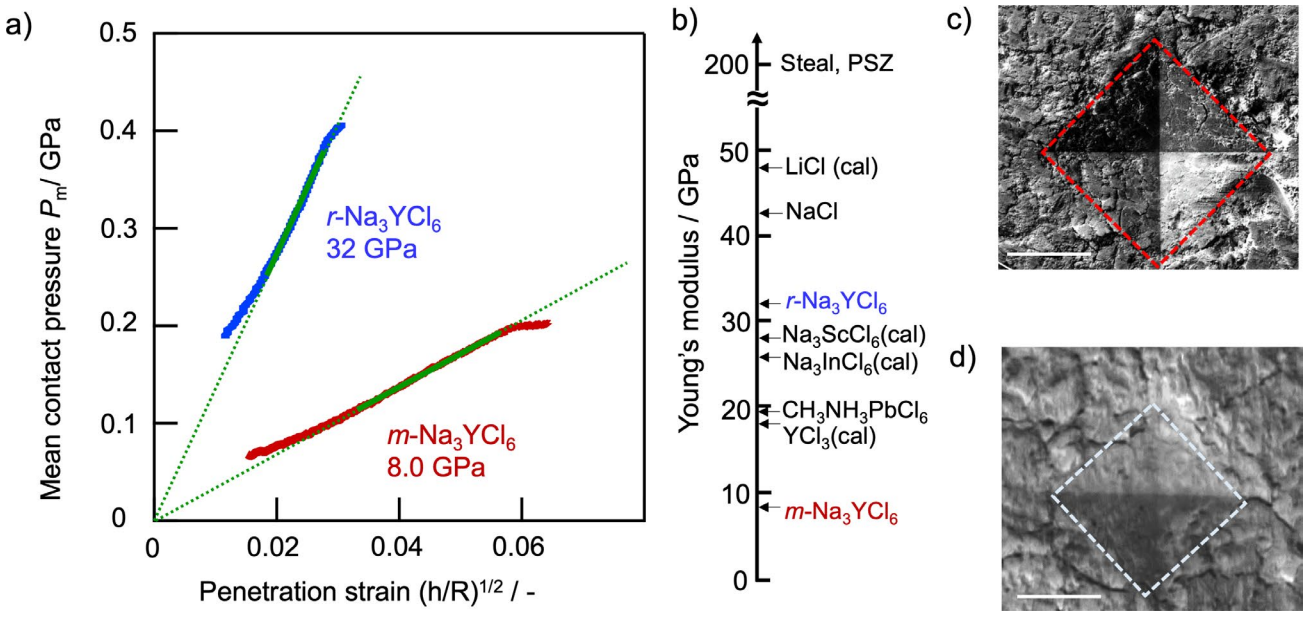

Figure 6. Mechanical properties of *m*- and *r*-Na_3YCl_6 pellets. a) Mean contact pressure curves and fitting curves of spherical indentations of *r*- and *m*-Na_3YCl_6 pellets. The relative density of both the pellets is 89 %. b) Comparison of Young's modulus of

Na_3YCl_6 with that of other halides,[24-28] steel, and PSZ. Scanning electron microscope images of the indentation impressions on c) *m*-Na_3YCl_6 and d) *r*-Na_3YCl_6; the white scale bar represents 100 μm.

Fig. 6(a) shows the mean contact pressure curves of *m*- and *r*-Na_3YCl_6 pellets obtained from the indentation measurements. The *m*-phase of Na_3YCl_6 has a lower yield point (0.20 GPa) than the *r*-phase (0.39 GPa), as calculated from the point at which the mean contact pressure is no longer proportional to the penetration strain. The Young's modulus of the *m*-phase calculated from the slope of the mean contact pressure curve is 8.0 GPa, which is a quarter of that of the *r*-phase (32 GPa). A low Young's modulus with high-density contradicts the general trend as observed in Ashby plots.[29] The Young's modulus of the *m*-phase is the lowest among that of typical chlorides such as[24,25] YCl_3,[26] Na_3ScCl_6,[28] Na_3InCl_6,[28] and perovskite chloride $CH_3NH_3PbCl_3$[27] (Fig. 6(b)). Therefore, *m*-Na_3YCl_6 is extremely soft even though it has a high density. The Young's modulus of *m*-Na_3YCl_6 calculated by the differentiation of the potential energy is 23 GPa, which is larger than the experimental value. This suggests that the low Young's modulus of *m*-Na_3YCl_6 is not the inherent characteristic of the structure itself; the dynamic *m*-to-*r* phase transformation makes the *m*-phase soft. The SEM images in Figs. 6c and d show that the indentation impression of the *m*-phase is larger than that of the *r*-phase, suggesting the high deformability of the *m*-phase. The presence of microcracks all over the pellet region indicates that the cracks did not originate from the indentation tests.

The low Young's modulus of *m*-Na_3YCl_6 is inconsistent with its high bulk modulus. Thus, the mechanical softness arises from the stress-induced martensitic phase transition of *m*- to *r*-Na_3YCl_6. Lateral expansion parallel to the indenters and the formation of small particles during the phase transformation may account for its softness and deformability. Further investigation using in-situ measurements is necessary to clarify the indentation-induced phase transformation of Na_3YCl_6.[30, 31] The effect of grain size on the phase transformation, as reported for PSZ,[32] will be studied in the future.

4. Conclusions

We discovered stress-induced martensite transformation of *m*-Na_3YCl_6 into *r*-Na_3YCl_6 with a significant volume expansion. In-situ XRD studies clarified that uniaxial pressure is essential for this transformation. Computational calculations indicated that an external force along the specific axis of *m*-Na_3YCl_6 induced the martensitic transformation with anisotropic volume expansion parallel to the force via a low kinetic barrier. The *m*-Na_3YCl_6 showed a large indentation impression and low Young's modulus, whereas a high bulk modulus was obtained from in-situ XRD measurements. This contradictory relationship between the Young's modulus and bulk modulus may be attributed to the martensitic transformation.

As a general summary, we propose the following requirements for achieving unusual chlorides with exciting mechanical properties, offering a framework for their application to other non-oxide materials. First, the material must be metastable against another polymorph. Remnant metastability is the concept of preparing a metastable polymorph, which was once the most stable phase under specific thermodynamic conditions and is then trapped upon rapidly changing the conditions.[5, 33] Second, the kinetic barrier of the martensitic transformation between the two polymorphs should be sufficiently small to stabilize both the phases near the ambient temperature, yet susceptible to reduction by anisotropic mechanical stimulation. Third, a combination of a denser metastable phase and sparser stable phase is essential to realize the volume expansion. Although this combination might seem counterintuitive, β-Sn/α-Sn[34] and diamond/graphite[35] are prime examples. In our case, this was accomplished through partially occupied sites, which are also observed in numerous non-oxide materials. By satisfying these requirements, martensitic transformations can be achieved even in highly ionic crystals, leading to intriguing mechanical properties that

can be predicted using computational frameworks. Moreover, the low symmetry of *m*-Na_3YCl_6, unlike tetragonal ZrO_2 in PSZ, suggests that a simple structure is not the requirement for exploring similar phase-transition-triggered materials. Therefore, the findings of this study can be applied to various non-oxide materials with complicated structures, including nitrides, sulfides, chlorides, and mix-anion compounds for applications in optics, electronics, and energy devices.[36, 37] The highly anisotropic phase transformation with a large volume expansion has the potential to improve the mechanical properties of halides and other non-oxides for the development of more processable and reliable future materials.

ASSOCIATED CONTENT

Supporting Information

Rietveld refinement profiles, electron diffraction profiles, XRD patterns with different temperatures and pressures, and computational details.

AUTHOR INFORMATION

Corresponding Author: **amirua@eng.hokudai.ac.jp (AMiura) , muraok_k@chemsys.t.u-tokyo.ac.jp (KMuraoka)**

A.Miura and K.Muraoka contributed equally.

ACKNOWLEDGEMENT

A.Miura thanks Prof. Daigo Miyajima (The Chinese University of Hong Kong) for valuable comments and discussion. This research was partially supported by KAKENHI Grant Numbers JP20KK0124, 21K20551, and 22K14751, and JST PRESTO (Grant Numbers JPMJPR21Q8 and JPMJPR21Q2) and JST GteX JPMJGX23S5. Part of the DFT calculations was performed on supercomputers at CCMS, IMR (Tohoku Univ., proposal no. 202212-SCKXX-0002)

References

(1) Asano, T.; Sakai, A.; Ouchi, S.; Sakaida, M.; Miyazaki, A.; Hasegawa, S. Solid Halide Electrolytes with High Lithium-Ion Conductivity for Application in 4 V Class Bulk-Type All-Solid-State Batteries. *Adv Mater* **2018**, *30* (44), e1803075. DOI: 10.1002/adma.201803075.

(2) Cheng, M.; Jiang, J.; Yan, C.; Lin, Y.; Mortazavi, M.; Kaul, A. B.; Jiang, Q. Progress and Application of Halide Perovskite Materials for Solar Cells and Light Emitting Devices. *Nanomaterials (Basel)* **2024**, *14* (5). DOI: 10.3390/nano14050391 From NLM PubMed-not-MEDLINE.

(3) Tsuji, M.; Sasase, M.; Iimura, S.; Kim, J.; Hosono, H. Room-Temperature Solid-State Synthesis of Cs(3)Cu(2)I(5) Thin Films and Formation Mechanism for Its Unique Local Structure. *J Am Chem Soc* **2023**, *145* (21), 11650-11658. DOI: 10.1021/jacs.3c01713 From NLM PubMed-not-MEDLINE.

(4) Huang, Z.; Yoshida, S.; Akamatsu, H.; Hayashi, K.; Ohno, S. NaMCl6 (M = Nb and Ta): A New Class of Sodium-Conducting Halide-Based Solid Electrolytes. *ACS Materials Letters* **2024**, 1732-1738. DOI: 10.1021/acsmaterialslett.4c00315.

(5) Ito, H.; Nakahira, Y.; Ishimatsu, N.; Goto, Y.; Yamashita, A.; Mizuguchi, Y.; Moriyoshi, C.; Toyao, T.; Shimizu, K.-i.; Oike, H.; et al. Stability and Metastability of Li_3YCl_6 and Li_3HoCl_6. *Bulletin of the Chemical Society of Japan* **2023**, *96* (11), 1262-1268. DOI: 10.1246/bcsj.20230132.

(6) Dai, T.; Wu, S.; Lu, Y.; Yang, Y.; Liu, Y.; Chang, C.; Rong, X.; Xiao, R.; Zhao, J.; Liu, Y.; et al. Inorganic glass electrolytes with polymer-like viscoelasticity. *Nature Energy* **2023**, *8* (11), 1221-1228. DOI: 10.1038/s41560-023-01356-y.

(7) Chevalier, J.; Liens, A.; Reveron, H.; Zhang, F.; Reynaud, P.; Douillard, T.; Preiss, L.; Sergo, V.; Lughi, V.; Swain, M.; et al. Forty years after the promise of «ceramic steel?»: Zirconia‐based composites with a metal‐like mechanical behavior. *Journal of the American Ceramic Society* **2019**, *103* (3), 1482-1513. DOI: 10.1111/jace.16903.

(8) Kriven, W. M. Possible Alternative Transformation Toughened Zirconia: Crystallographic Aspects. *Journal of the American Ceramic Society* **1988**, *71* (12), 1021-1030. DOI: https://doi.org/10.1111/j.1151-2916.1988.tb05786.x.

(9) Meyer, G.; Peter Ax, S.; Schleid, T.; Irmler, M. The chlorides Na3MCl6 (M □ Eu□Lu, Y, Sc): Synthesis, crystal structures, and

thermal behaviour. *Zeitschrift für anorganische und allgemeine Chemie* **1987**, *554* (11), 25-33. DOI: https://doi.org/10.1002/zaac.19875541104.

(10) Wu, E. A.; Banerjee, S.; Tang, H.; Richardson, P. M.; Doux, J. M.; Qi, J.; Zhu, Z.; Grenier, A.; Li, Y.; Zhao, E.; et al. A stable cathode-solid electrolyte composite for high-voltage, long-cycle-life solid-state sodium-ion batteries. *Nat Commun* **2021**, *12* (1), 1256. DOI: 10.1038/s41467-021-21488-7.

(11) Liao, W.; Dronskowski, R. Trisodium yttrium(III) hexachloride. *Acta Crystallographica Section E Structure Reports Online* **2004**, *60* (6), i72-i73. DOI: 10.1107/s1600536804011043.

(12) Stenzel, F.; Meyer, G. Ternäre Halogenide vom Typ A3MX6. II. Das System Ag3−xNaxYCl6: Synthese, Strukturen, Ionenleitfähigkeit. *Zeitschrift für anorganische und allgemeine Chemie* **1993**, *619* (4), 652-660. DOI: https://doi.org/10.1002/zaac.19936190406.

(13) Patil, R. N.; Subbarao, E. C. Axial thermal expansion of ZrO_2 and HfO_2 in the range room temperature to 1400°C. *Journal of Applied Crystallography* **1969**, *2* (6), 281-288. DOI: https://doi.org/10.1107/S0021889869007217.

(14) Momma, K.; Izumi, F. VESTA: a three-dimensional visualization system for electronic and structural analysis. *J. Appl. Crystallogr.* **2008**, *41* (3), 653-658. DOI: doi:10.1107/S0021889808012016.

(15) Coelho, A. A. TOPAS and TOPAS-Academic: an optimization program integrating computer algebra and crystallographic objects written in C++. *Journal of Applied Crystallography* **2018**, *51* (1), 210-218. DOI: 10.1107/s1600576718000183.

(16) Kawaguchi, S.; Takemoto, M.; Osaka, K.; Nishibori, E.; Moriyoshi, C.; Kubota, Y.; Kuroiwa, Y.; Sugimoto, K. High-throughput powder diffraction measurement system consisting of multiple MYTHEN detectors at beamline BL02B2 of SPring-8. *Rev Sci Instrum* **2017**, *88* (8), 085111. DOI: 10.1063/1.4999454.

(17) Hikima, K.; Totani, M.; Obokata, S.; Muto, H.; Matsuda, A. Mechanical Properties of Sulfide-Type Solid Electrolytes Analyzed by Indentation Methods. *ACS Applied Energy Materials* **2022**, *5* (2), 2349-2355. DOI: 10.1021/acsaem.1c03829.

(18) Sheppard, D.; Xiao, P.; Chemelewski, W.; Johnson, D. D.; Henkelman, G. A generalized solid-state nudged elastic band method. *The Journal of Chemical Physics* **2012**, *136* (7). DOI: 10.1063/1.3684549 (acccessed 4/26/2023).

(19) Takamoto, S.; Shinagawa, C.; Motoki, D.; Nakago, K.; Li, W.; Kurata, I.; Watanabe, T.; Yayama, Y.; Iriguchi, H.; Asano, Y.; et al. Towards universal neural network potential for material discovery applicable to arbitrary combination of 45 elements. *Nat Commun* **2022**, *13* (1), 2991. DOI: 10.1038/s41467-022-30687-9 From NLM Medline.

(20) Stevanović, V.; Trottier, R.; Musgrave, C.; Therrien, F.; Holder, A.; Graf, P. Predicting kinetics of polymorphic transformations from structure mapping and coordination analysis. *Physical Review Materials* **2018**, *2* (3). DOI: 10.1103/PhysRevMaterials.2.033802.

(21) Kresse, G.; Furthmüller, J. Efficient iterative schemes for ab initio total-energy calculations using a plane-wave basis set. *Physical Review B* **1996**, *54* (16), 11169-11186.

(22) Ong, S. P.; Richards, W. D.; Jain, A.; Hautier, G.; Kocher, M.; Cholia, S.; Gunter, D.; Chevrier, V. L.; Persson, K. A.; Ceder, G. Python Materials Genomics (pymatgen): A robust, open-source python library for materials analysis. *Computational Materials Science* **2013**, *68*, 314-319. DOI: 10.1016/j.commatsci.2012.10.028.

(23) Maki, K.; Muraoka, K.; Kawaguchi, S.; Tanimoto, T.; Nakayama, A.; Yokokura, S.; Shimada, T.; Tadanaga, K.; Miura, A. High-pressure phase and pressure-induced phase transition of Ag3YCl6. *CrystEngComm* **2024**, *26* (13), 1814-1818. DOI: 10.1039/d3ce01185b.

(24) Anderson, O. L. 2 - Determination and Some Uses of Isotropic Elastic Constants of Polycrystalline Aggregates Using Single-Crystal Data. In *Physical Acoustics*, Mason, W. P. Ed.; Vol. 3; Academic Press, 1965; pp 43-95.

(25) Duncan-Hewitt, W. C.; Weatherly, G. C. Evaluating the hardness, Young's modulus and fracture toughness of some pharmaceutical crystals using microindentation techniques. *Journal of Materials Science Letters* **1989**, *8* (11), 1350-1352. DOI: 10.1007/BF00721518.

(26) Wu, M.; Cui, J.; Yang, W.; Dai, H.; Dong, H.; Cheng, Y.; Hong, Z.; Wang, W.; Lu, F.; Liu, H.; et al. Two-Dimensional Protective Layers of MX3 to Stabilize Lithium and Sodium Metal Anodes. *ACS Applied Energy Materials* **2021**, *4* (8), 8653-8659. DOI: 10.1021/acsaem.1c01903.

(27) Sun, S.; Fang, Y.; Kieslich, G.; White, T. J.; Cheetham, A. K. Mechanical properties of organic–inorganic halide perovskites, CH3NH3PbX3(X = I, Br and Cl), by nanoindentation. *Journal of*

Materials Chemistry A **2015**, *3* (36), 18450-18455. DOI: 10.1039/c5ta03331d.

(28) Lian, Y.; Wu, M.; Xu, B.; He, B.; Liu, G.; Shi, J.; Kuang, Q.; Wang, H.; Ouyang, C. Phase-structure design for sodium chloride solid electrolytes with outstanding performance: a first-principles approach. *Journal of Materials Chemistry A* **2023**, *11* (4), 1906-1919. DOI: 10.1039/d2ta07603a.

(29) Ashby, M. F.; Cebon, D. Materials selection in mechanical design. *J. Phys. IV France* **1993**, *03 (C7)*, C7-1-C7-9.

(30) Gerbig, Y. B.; Michaels, C. A.; Bradby, J. E.; Haberl, B.; Cook, R. F. In situ spectroscopic study of the plastic deformation of amorphous silicon under nonhydrostatic conditions induced by indentation. *Physical Review B* **2015**, *92* (21), 214110. DOI: 10.1103/PhysRevB.92.214110.

(31) Yoshida, S.; Nguyen, T. H.; Yamada, A.; Matsuoka, J. In-Situ Raman Measurements of Silicate Glasses during Vickers Indentation. *MATERIALS TRANSACTIONS* **2019**, *60* (8), 1428-1432. DOI: 10.2320/matertrans.MD201901.

(32) HEUER, A. H.; CLAUSSEN, N.; KRIVEN, W. M.; RUHLE, M. Stability of Tetragonal ZrO2 Particles in Ceramic Matrices. *Journal of the American Ceramic Society* **1982**, *65* (12), 642-650. DOI: https://doi.org/10.1111/j.1151-2916.1982.tb09946.x.

(33) Sun, W.; Dacek, S. T.; Ong, S. P.; Hautier, G.; Jain, A.; Richards, W. D.; Gamst, A. C.; Persson, K. A.; Ceder, G. The thermodynamic scale of inorganic crystalline metastability. *Science advances* **2016**, *2* (11), e1600225-e1600225. DOI: 10.1126/sciadv.1600225 PubMed.

(34) Nogita, K.; Gourlay, C. M.; McDonald, S. D.; Suenaga, S.; Read, J.; Zeng, G.; Gu, Q. F. XRD study of the kinetics of $\beta \leftrightarrow \alpha$ transformations in tin. *Philosophical Magazine* **2013**, *93* (27), 3627-3647. DOI: 10.1080/14786435.2013.820381.

(35) Bundy, F. P.; Bassett, W. A.; Weathers, M. S.; Hemley, R. J.; Mao, H. U.; Goncharov, A. F. The pressure-temperature phase and transformation diagram for carbon; updated through 1994. *Carbon* **1996**, *34* (2), 141-153. DOI: https://doi.org/10.1016/0008-6223(96)00170-4.

(36) Rivadulla, F.; Banobre-Lopez, M.; Quintela, C. X.; Pineiro, A.; Pardo, V.; Baldomir, D.; Lopez-Quintela, M. A.; Rivas, J.; Ramos, C. A.; Salva, H.; et al. Reduction of the bulk modulus at high pressure in CrN. *Nat Mater* **2009**, *8* (12), 947-951. DOI: 10.1038/nmat2549 From NLM PubMed-not-MEDLINE.

(37) Kageyama, H.; Hayashi, K.; Maeda, K.; Attfield, J. P.; Hiroi, Z.; Rondinelli, J. M.; Poeppelmeier, K. R. Expanding frontiers in materials chemistry and physics with multiple anions. *Nat Commun* **2018**, *9* (1), 772. DOI: 10.1038/s41467-018-02838-4.

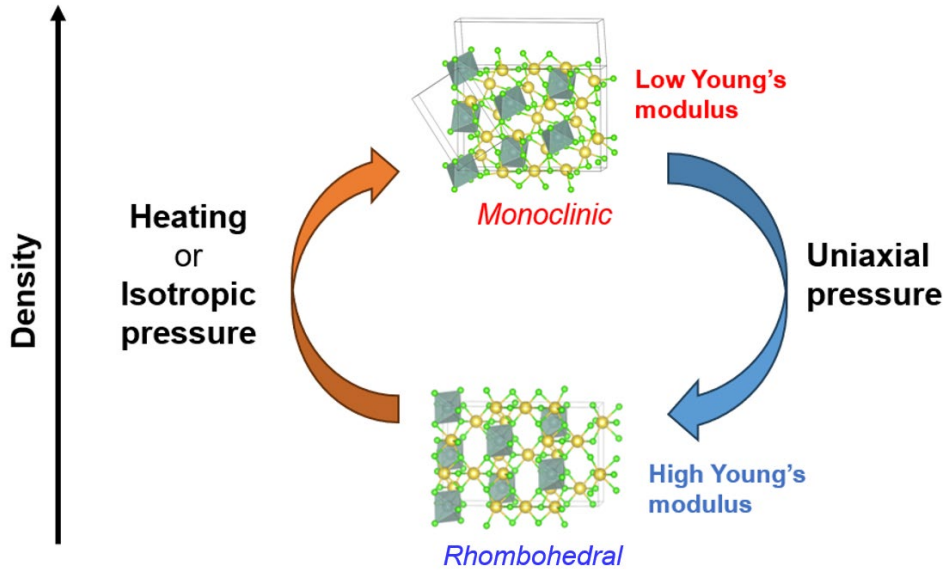
Density
Heating
or
Isotropic
pressure
Low Young's
modulus
Monoclinic
Uniaxial
pressure
High Young's
modulus
Rhombohedral